14th International Symposium on Turbulence and Shear Flow Phenomena (TSFP14)
Heidelberg, Germany, July 28–31, 2026

DATA-DRIVEN FORCING-INFORMED RESOLVENT ANALYSIS

Yuta Iwatani
Department of Aerospace Engineering
Graduate School of Engineering
Tohoku University
Miyagi, 980-0845, Japan
yuta.iwatani@tohoku.ac.jp

Kunihiko Taira
Department of Mechanical and Aerospace Engineering
University of California, Los Angeles
CA 90095, USA
ktaira@seas.ucla.edu

Soshi Kawai
Department of Aerospace Engineering
Graduate School of Engineering
Tohoku University
Miyagi, 980-0845, Japan
kawai@tohoku.ac.jp

ABSTRACT

We present a forcing-informed (FI) resolvent analysis, a framework for extracting the input-output relations of self-sustained, statistically stationary nonlinear flows. The key idea behind the present approach is to estimate the basis of the subspace spanned by the time history of the nonlinear forcing (input subspace), as well as that of the output subspace. The learned bases are used to construct a new transfer function matrix, called the forcing-informed (FI) resolvent operator, which is founded on the self-sustained flows. In the FI resolvent analysis, the extracted forcing and response modes are theoretically grounded to exist in the actual flow field, in contrast to conventional resolvent analysis. In addition, the time history of the nonlinear forcing can also be used to estimate the linear operator, thereby allowing us to obtain the FI resolvent operator in a fully data-driven manner. The proposed method is demonstrated for a 2D cylinder wake and a 3D transitional boundary layer, while addressing the role of the nonlinear forcing term in nonlinear energy transfer in these flows.

INTRODUCTION

Uncovering self-sustaining mechanisms is crucial for elucidating the intrinsic dynamics of complex nonlinear flows and for controlling them with enhanced insights. However, identifying self-sustaining mechanisms from numerical simulation data is challenging, even with the availability of high-fidelity simulation datasets, because of the nonlinear and complex behavior of fluid flows. Thus, a method capable of identifying such a mechanism is desirable.

Resolvent analysis (Trefethen *et al.*, 1993; Jovanović & Bamieh, 2005; McKeon & Sharma, 2010) has served as a powerful tool for understanding (Iwatani *et al.*, 2023), modeling (Gómez *et al.*, 2016), and controlling (Yeh *et al.*, 2020) flows by identifying input-output relations in the flow field of interest. The effectiveness of the resolvent analysis has been demonstrated, even for turbulent base flows (McKeon & Sharma, 2010), thereby attracting the interest of the fluid mechanics community to date. The key concept in McKeon & Sharma (2010) is the feedback mechanism, which reinterprets the nonlinear forcing term in the linearized Navier–Stokes (NS) equations around the time-averaged flow as an exogenous forcing to the linear system (Farrell & Ioannou, 1993). The nonlinear forcing term is viewed as an essential feedback controller that maintains the oscillatory motions of self-sustained flows. However, the resolvent operator lacks the full spatiotemporal characteristics of the nonlinear forcing terms; only the mean flow modification due to the time-averaged nonlinear fluctuation component of the NS equation, that is, the Reynolds stress, can inform the resolvent operator of the nonlinear forcing. It has been pointed out that this lack of forcing information often leads to response and forcing modes inconsistent with the actual flow (e.g., Zare *et al.* (2017); Towne *et al.* (2018)).

Hence, in this study, we develop an input-output analysis method for (statistically stationary) nonlinear flows that incorporates forcing information, aiming to understand the mechanisms underlying self-sustained flow dynamics. The proposed method is applied to a two-dimensional cylinder flow at a Reynolds number of 150 and a three-dimensional controlled (H-type) transition in a high-subsonic boundary layer. The physical interpretations of the extracted forcing and response modes for these example flows are discussed.

FORCING-INFORMED RESOLVENT ANALYSIS
Fundamentals

Let us consider the Reynolds decomposed compressible NSEs and the Reynolds-averaged NS (RANS) written as

$$\partial_t \bar{q} + \partial_t q' = N(\bar{q}) + Lq' + F(q'), \tag{1}$$
$$\overline{\partial_t q} = \overline{N(q)} = N(\bar{q}) + \overline{F(q')}. \tag{2}$$

Here, q' denotes the perturbation of the state vector, L is the linearized Navier–Stokes operator, and $F(q')$ collects the nonlinear terms. Subtracting Eq. (2) from Eq. (1) gives the nonlinear perturbation equation as

$$\partial_t q' = Lq' + f'_{\mathrm{NL}}(q'), \tag{3}$$

where $f'_{\mathrm{NL}}(q') := F(q') - \overline{F(q')}$ is the zero-mean nonlinear term. Note that f'_{NL} is computable since the expression is available for this governing equation, which is revisited later. The Fourier transform of Eq. (3) yields a relation at a frequency ω:

$$\hat{q}_\omega = R\hat{f}_\omega, \tag{4}$$

where $R = [i\omega I - L]^{-1}$ is the resolvent operator, $\hat{q}_\omega$ and $\hat{f}_\omega$ are the Fourier coefficients of the q' and f'_{NL}. Note that we may also consider a general integral transformation (such as the Laplace and wavelet transforms). The choice of kernel function in the integral transform determines the temporal structure of the forcing and response modes, as discussed in the resolvent analysis literature (Yeh *et al.*, 2020; Ballouz *et al.*, 2024). We restrict ourselves to the harmonic response and forcing modes (they vary according to $e^{i\omega t}$) in this study.

In the conventional resolvent analysis, the forcing and response modes are given as the solution to the following optimization problem:

$$\max_{\hat{f}_\omega \neq 0} \frac{\|\hat{q}_\omega\|^2}{\|\hat{f}_\omega\|^2} = \max_{\hat{f}_\omega \neq 0} \frac{\|R_\omega \hat{f}_\omega\|^2}{\|\hat{f}_\omega\|^2}, \tag{5}$$

where $\|\cdot\| := \sqrt{\langle \cdot,\cdot \rangle}$ is the 2-norm of a vector. The SVD of the resolvent operator R solves the maximization problem (5); choosing $\hat{f}_\omega = v_{R,1}$ (the right singular vector $v_{R,1}$ that corresponds the leading singular value $\sigma_1(R)$) gives the maximum gain $\sigma_1(R)$ and the corresponding response $u_{R,1}$ which is the left singular vector. However, as pointed out in prior studies (Zare *et al.*, 2017; Taira *et al.*, 2017; Towne *et al.*, 2018; Morra *et al.*, 2021; Nogueira *et al.*, 2021; Barthel *et al.*, 2021), the forcing and response modes obtained by the SVD of $\mathbf{R}$ often fail to extract the flow structure that actually exists in the flow field from numerical simulations or experiments due to the lack of information (spatiotemporal coherence) about the nonlinear forcing term f'_{NL} in Eq. (3). In terms of linear algebra, although the (5) seems to maximize the gain between the nonlinear forcing $\hat{f}_\omega$ and response $\hat{q}_\omega$, the maximization problem of the Rayleigh quotient merely searches the surface of the unit sphere in vector space $\mathbb{C}^{N_q}$ (arbitrary orientation) for the optimum solution, regardless of the actual spatial correlation of $\hat{f}_\omega$. In other words, there is no theoretical guarantee that the optimal solution to (5) reflects the actual forcing information. Hence, let us consider how to incorporate the actual spatiotemporal structure of the nonlinear forcing term into the input-output analysis framework hereafter.

Basis estimation

The heart of this proposed method is to estimate the basis vectors of the input subspace spanned by the time-series data of the nonlinear forcing term, while benefiting from high-fidelity simulation data. To do so, let us collect snapshots and create the data matrix of forcing X:

$$X := \left[\ \underline{f'^{(1)}_{\mathrm{NL},1}, \cdots f'^{(1)}_{\mathrm{NL},M}}, \ldots, \underline{f'^{(N_p)}_{\mathrm{NL},1}, \ldots, f'^{(N_p)}_{\mathrm{NL},M}}\ \right], \tag{6}$$

where N_p is the number of the realizations, e.g., the number of the run of the numerical simulation or the number of the sets of the snapshot separated by a finite time window as in Welch's method (Welch, 2003). Here, M is the number of snapshots in each realization. Similarly, let us consider the data matrix of response Y:

$$Y := \left[\ \underline{q'^{(1)}_1, \ldots q'^{(1)}_M}, \ldots, \underline{q'^{(N_p)}_1, \ldots, q'^{(N_p)}_M}\ \right]. \tag{7}$$

Using these data matrices, the input and output subspaces are defined as $\mathscr{V}_\Phi := \mathrm{Col}(X)$ and $\mathscr{V}_\Psi := \mathrm{Col}(Y)$, respectively, where $\mathrm{Col}[\cdot]$ denotes the column space of a matrix. Since we are now interested in the frequency domain as in Eq. (4), by performing the Fourier transform of every realization of X and Y, we may obtain the following matrices,

$$\widehat{X}(\omega) = \left[\hat{f}_1(\omega), \cdots \hat{f}_{N_p}(\omega)\right], \tag{8}$$

$$\widehat{Y}(\omega) = \left[\hat{q}_1(\omega), \cdots \hat{q}_{N_p}(\omega)\right], \tag{9}$$

at every frequency of ω. For each, the input and output subspaces are given as $\mathscr{V}_{\Phi(\omega)} := \mathrm{Col}[\hat{X}(\omega)] \subseteq \mathscr{V}_\Phi$ and $\mathscr{V}_{\Psi(\omega)} := \mathrm{Col}[\hat{Y}(\omega)] \subseteq \mathscr{V}_\Psi$, respectively. In general, the basis vectors of these two subspaces are given by the rank factorization of $\widehat{X}$ and $\widehat{Y}$ for each, written as

$$\widehat{X} = \Phi C, \quad \widehat{Y} = \Psi D. \tag{10}$$

Here, $\Phi \in \mathbb{C}^{N_q \times N_\Phi}$ and $\Psi \in \mathbb{C}^{N_q \times N_\Psi}$ are the sets of basis vectors as many as the rank of $\widehat{X}$ and $\widehat{Y}$, and $C \in \mathbb{C}^{N_\Phi \times N_\Phi}$ and $D \in \mathbb{C}^{N_\Psi \times N_\Psi}$ are the coefficient matrix. From Eq. (10), the column vectors of Φ and Ψ apparently span the input and output subspaces, respectively. Note that the rank factorization is merely a mathematical expression; there are several practical numerical algorithms to reveal the rank of a matrix, such as the singular value decomposition (SVD). In addition, noticing that the f'_{NL} and q' can be recovered as

$$f'_{\mathrm{NL}} = \int_{-\infty}^{\infty} \Phi(\omega)C(\omega)e^{i\omega t}d\omega, \tag{11}$$

$$q' = \int_{-\infty}^{\infty} \Psi(\omega)D(\omega)e^{i\omega t}d\omega, \tag{12}$$

we can view this decomposition as a general expression of the modal decomposition of a flow field, in which the temporal coherence and spatial coherence are considered separately (Taira *et al.*, 2017). Since the temporal coherence is now described by $e^{i\omega t}$, the spectral proper orthogonal (SPOD) decomposition (corresponding to the SVD of $\widehat{X}$ and $\widehat{Y}$) and the dynamic mode decomposition (DMD) method may be applied, for example. As such, there are several numerical methods to obtain the basis vectors of input and output subspaces, including the modern modal decomposition methods. In this study, we use the SPOD to obtain the bases, allowing us to express the vectors $\hat{q}$ and $\hat{f}$ as

$$\hat{f}_\omega = \Phi_{\mathrm{spod}}\Sigma_\phi a, \ \ \hat{q}_\omega = \Psi_{\mathrm{spod}}\Sigma_\psi b, \tag{13}$$

where Φ_{spod} and Ψ_{spod} are the orthonormal SPOD modes, and Σ_ϕ and Σ_ψ are diagonal matrices whose entries indicate the amplitude of SPOD modes (basis vectors). Here, a and b are coefficient vectors with unit norm. In this sense, the data-driven resolvent analysis (Herrmann *et al.*, 2021) uses the DMD basis of output q' for both input and output subspaces, i.e., $q' = \Psi_{\mathrm{DMD}} a$, $f'_{\mathrm{NL}} = \Psi_{\mathrm{DMD}} b$.

Forcing-informed resolvent operator

Using the learned bases, let us derive the proposed forcing-informed (FI) resolvent operator G. From the FI resolvent operator G, we will extract the input and output modes theoretically grounded to exist in the actual flow field. To derive the FI-resolvent operator, we sustitude Eq. (13) into Eq. (4) to arrive at

$$\Sigma_\psi b = Ga, \tag{14}$$

where

$$G := \Psi^*_{\mathrm{spod}} R \Phi_{\mathrm{spod}} \Sigma_\phi, \tag{15}$$

is the FI resolvent operator, since G knows the spatiotemporal correlation of the nonlinear forcing term $\Phi_{\mathrm{spod}}\Sigma_\Phi$. Using the SVD of the FI resolvent operator $G \underset{SVD}{=} \sum u_{G,j} \Sigma_{G,j} V^*_{G,j}$ ($\sigma_{G,k} \geq \sigma_{G,k+1}$) and Eq. (13), the most dominant response and forcing mode can be recovered as

$$\begin{aligned} \hat{q}_{\mathrm{resp}} &= \Psi_{\mathrm{spod}} \Sigma_\psi a \underset{\text{Eq. (14)}}{=} \Psi_{\mathrm{spod}} G a \underset{a = v_{G,1}}{=} \Psi_{\mathrm{spod}} u_{G,1} \sigma_{G,1}, \\ \hat{f}_{\mathrm{forc}} &= \Phi_{\mathrm{spod}} \Sigma_\phi v_{G,1}, \end{aligned} \tag{16}$$

respectively. In the above equation, we choose $a = v_{G,1}$, which is justified since a is a free vector with unit norm. We refer to the modes (Eq. (16)) obtained by FI resolvent analysis as the FI response and forcing modes. This pair of FI forcing and response modes is the dominant input-output relation governing the self-sustaining flow of interest. These FI resolvent modes exist in the actual flow field since they are expressed as linear combinations of the basis vectors of input and output subspaces, respectively. Finally, when the FI resolvent operator is a rank-1 matrix, the amplitude of the output Σ_ψ coincides with the leading singular value $\sigma_{G,1}$, as demonstrated later.

Data-driven estimation of linear operator

The FI resolvent operator G requires the three matrices, Φ, Ψ, and L, to be available. As the former two are obtained using SPOD, estimating L in a data-driven manner completes the overall data-driven formulation. Based on Eq. (3), the linear operator is approximated as

$$L \approx L_{\mathrm{data}} = [\dot{Y} - X] Y^\dagger \tag{17}$$

where $\dot{Y}$ collects the snapshots of the time derivatives of the output dq'/dt, $Y^\dagger$ is the pseudo-inverse of Y. Once we compute $Z := \dot{Y} - X$, the same algorithm used in the (projected) DMD (Schmid, 2010) (or its parallelized version (Asada & Kawai, 2025)) is applicable. Finally, the FI resolvent operator is constructed in a full-data-driven manner as $G_{\mathrm{data}} = \Phi^*_{\mathrm{spod}} U^r_X (i\omega I - L_r) U^{r\,*}_X \Psi_{\mathrm{spod}} \Sigma_\Psi$, where U^r_X is the r dominant left singular vectors of Y, that is, the POD modes and L_r is the linear operator projected on the first r POD modes. Obviously, the FI resolvent operator $G \in \mathbb{C}^{N_\Phi \times N_\Psi}$ is much smaller than the resolvent operator $R \in \mathbb{C}^{N_q \times N_q}$, reducing the computational cost of the SVD and saving on memory requirement.

Energy balance in the statistically stationary self-sustained flows

To relate the obtained forcing and response modes to the self-sustaining mechanisms, we follow the work by Jin *et al.* (2021), who considers the time-evolution equation of the disturbance energy defined as $E = \langle q', q' \rangle$. The time-averaged evolution equation of E is written as

$$\overline{\frac{dE}{dt}} = \overline{\langle q', Lq' \rangle} + \overline{\langle q', f'_{\mathrm{NL}} \rangle} = 0, \tag{18}$$

where $\bar{\cdot}$ denotes the time-averaging operation. Eq. (18) describes that the (long-time) energy amplification or attenuation due to the linear mechanism ($\overline{\langle q', Lq' \rangle}$) is being balanced with the counterpart of the nonlinear mechanisms ($\overline{\langle q', f'_{\mathrm{NL}} \rangle}$) in the self-sustained statistically stationary flows. In particular, the term $\overline{\langle q', f'_{\mathrm{NL}} \rangle}$ tells that the energy amplification/dissipation due to the nonlinear mechanism is determined by the phase difference (inner product) between q' and f'_{NL}. Similarly, in the frequency space, we may show that the phase difference between the response and forcing modes also tells the energy amplification/dissipation due to $\hat{f}_{\mathrm{forc}}$ at the frequency of interest. Thus, the real part of the Hadamard product

$$\mathscr{T} := \mathrm{Real}(\hat{q}_{\mathrm{resp}} \circ \hat{f}^*_{\mathrm{forc}}), \tag{19}$$

represents where the forcing amplifies or attenuates the output energy in the time-averaged sense.

RESULTS AND DISCUSSIONS

2D cylinder flow

We first consider the 2D cylinder flow at a diameter-based Reynolds number of $Re = 150$ and at a freestream Mach number of $M_\infty = 0.2$, which exhibits self-sustained Karman vortex shedding. The Strouhal number associated with the vortex shedding $St_K = fD/U_\infty \approx 0.18$, where f is the shedding frequency, D is the diameter, and U_∞ is the freestream velocity.

First, the eigenvalues of the linear operator L_{data} obtained from data by Eq. (17) are shown in Fig. 1. The most unstable eigenvalue L_{data} collapses onto one of the L obtained by direct computation (black cross), which indicates that the present data-driven method works appropriately. Although not shown here, the eigenvector exhibits the physical vortex-shedding mode, and the response and forcing modes shown later look almost the same regardless of the construction methods of the linear operator.

In Fig. 2, the gain (the leading singular value σ_1) of the proposed FI resolvent operator (green line) exhibits the peaks of the harmonics of St_K (i.e., $2St_K, 3St_K$), at which the linear mechanism is inactive (which can be judged from Fig. 1). On the other hand, the gain of the conventional resolvent operator (gray line) only possesses a peak at St_K. This result demonstrates that incorporating the spatiotemporal structure of the nonlinear forcing term f'_{NL} is necessary to capture the nonlinear amplification mechanisms. Besides the harmonics, the FI-resolvent gain at the fundamental frequency St_K matches the SPOD gain (orange crosses), while the gain of R overpredicts it. This gap reflects the fact that the amplitude of response mode is determined not only by the singular value of R but also the inner product between the right singular vector of R and the nonlinear forcing term $\hat{f}$ (Taira *et al.*, 2017).

Subsequently, the streamwise momentum component of the FI response and forcing modes from the FI resolvent operator G at St_K, $2St_K$, and $3St_K$ are shown in Fig. 3. The FI

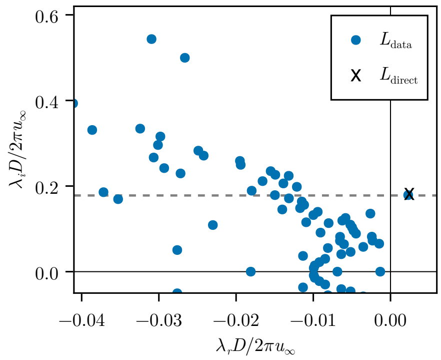

Figure 1. Eigenvalues of linear operator estimated in a data-driven manner L_{data} (blue circles), along with the most unstable eigenvalue of linear operator obtained by a direct computation L_{direct} (black cross).

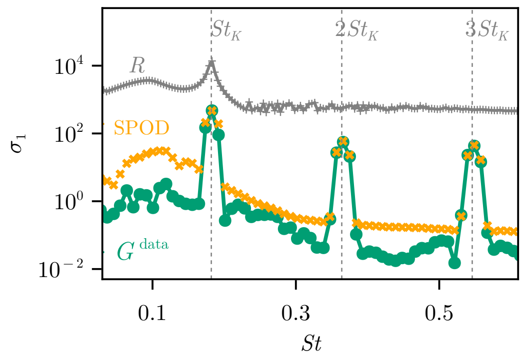

Figure 2. Gains of FI resolvent operator G (green), conventional resolvent operator R, and SPOD modes of output (orange cross).

response modes at the fundamental St_K and second-harmonic $2St_K$ frequencies are similar to the DMD modes at the corresponding frequencies (Taira *et al.*, 2020), indicating the present method extracts the physical modes. Comparing the FI response and forcing modes at St_K in Fig. 3 with the conventional resolvent analysis in Fig. 4, the response modes look similar to each other, whereas the shape of the forcing mode is different; the FI-forcing mode possesses the structure in the cylinder wake, while the conventional forcing mode emphasizes the region upstream of the cylinder. Since the forcing term $f'_{\text{NL}}(q')$ is the nonlinear function of q' (feedback controller), the FI-forcing mode should not appear upstream of the cylinder where no flow oscillation occurs. In addition, at $2St_K$, the FI-forcing mode is similar to the forcing mode that explicitly models the triadic interaction of $St_K + St_K = 2St_K$ (Rosenberg *et al.*, 2019), demonstrating that the proposed method can capture the nonlinear resonant mechanism.

Finally, we examine the spatial distribution of $\mathscr{T}$ in Fig. 3 (the bottom row). The region where the nonlinear forcing term supplies the energy to the output is visualized as a positive signed green colored region, whereas the region in which the forcing attenuates the energy is visualized as a negative signed pink colored domain. It is identified that the nonlinear forcing at St_K acts as the driving force in the recirculation region at around $0.5 < x/D < 2$, whereas it dissipates the energy in the region of the time-averaged separated shear layer considered as the source of linear instability. In the wake domain $(2 < x/D)$, $\mathscr{T}$ is negative (pink) at St_K, whereas it is almost positive (green) at harmonics $2St_K, 3St_K$, indicating that the nonlinear forcing term supplies energy to the wake region at these frequencies (harmonics), where the linear amplification mechanism is inactive.

3D transitional boundary layer

We then examine the 3D transitional boundary layer. The DNS data of the H-type transition in high-subsonic boundary layers at a Mach number of 0.8 over a nominally zero-pressure-gradient pseudo-adiabatic (isothermal) flat plate (`https://www.klab.mech.tohoku.ac.jp/database/index.html`) is analyzed. In the DNS, infinitesimal initial disturbances consisting of a two-dimensional Mack's first mode (Mack, 1975) at a frequency of ω_{2D} and its subharmonic oblique mode (Herbert, 1983) are introduced to trigger instabilities. For details of the DNS setup, the reader is referred to Iwatani *et al.* (2025). As shown in Fig. 5, we focus on the late stage of the transition, in which the three-dimensional characteristic vortices, such as the lambda-vortex and the ring-vortex, appear and evolve downstream nonlinearly.

The leading gain of the FI resolvent operator is shown in Fig. 6. The gain exhibits peaks not only at frequencies where the linear amplification mechanism is active ($|\omega/\omega_{2D}| < 2/3$), but also at frequencies where the nonlinear amplification mechanism is active ($|\omega/\omega_{2D}| > 2/3$). Here, the linear stability of this flow is analyzed through eigenvalue analysis of the linear operator estimated from data, and note that this is not the linear instability of Mack's mode and subharmonic instability. Hereafter, we examine the forcing and response modes at $\omega/\omega_{2D} = 1/2$ (active linear amplification) and $\omega/\omega_{2D} = 2$ (inactive linear amplification).

In Fig. 7, the spatial distributions of the streamwise momentum component of the forcing and response modes and the distribution of $\mathscr{T}$ in X-Z (wall-normal–spanwise) cross-section at the streamwise location of the ring vortices (corresponding to the dashed rectangle in Fig. 5) are shown. Looking at the response modes, we may find, for example, the characteristic modal structure at $X \approx 0.08$–0.1 at spanwise locations of $Z = 0.5N(N = 0, 1, 2\dots)$, corresponding to the ring-vortex (see also Fig. 5). In this way, the response modes reveal the coherent spatial structure in the late stage of the H-type transition. The forcing modes (middle column of Fig. 7) also exhibit coherent spatial structures at both frequencies, indicating that the nonlinear forcing terms play an essential role in shaping the coherent flow structure in the late stage of the transitional boundary layer. Finally, looking at the spatial distribution of $\mathscr{T}$ (the right column of Fig. 7), the negatively signed (purple) region largely coincides with the local peaks of the response mode's amplitude at $\omega/\omega_{2D} = 1/2$ (linearly unstable). The positional relation indicates that the nonlinear forcing decays the fluctuation energy amplified by the linear instability. In contrast, $\omega/\omega_{2D} = 2$ (linearly stable), the area of the green-colored region (nonlinear energy amplification) expands relative to the area at $\omega/\omega_{2D} = 1/2$, indicating that the nonlinear amplification mechanism becomes predominant, especially in regions away from the wall. Through the FI resolvent analysis, the spatial structure of the nonlinear forcing term and the role of the forcing at a specific location in the self-sustaining mechanism of the late stage of the H-type transition are identified.

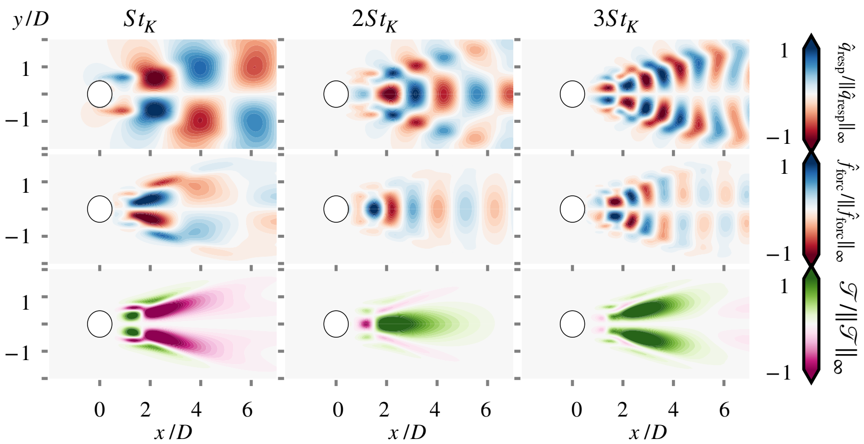

Figure 3. Results of the FI resolvent analysis of cylinder wake: (top) streamwise momentum component of the FI response mode, (middle) FI forcing mode, and (bottom) spatial distribution of $\mathscr{T}$ (Eq. (19)), at $St = St_K$ (left), $2St_K$ (middle), and $3St_K$ (right).

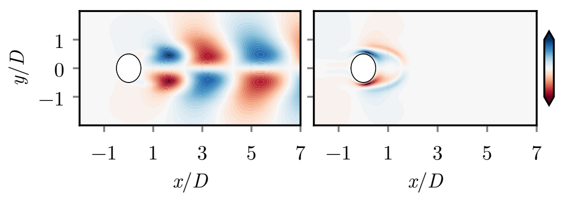

Figure 4. Streamwise momentum component of response (left) and forcing (right) modes from the resolvent operator R at St_K.

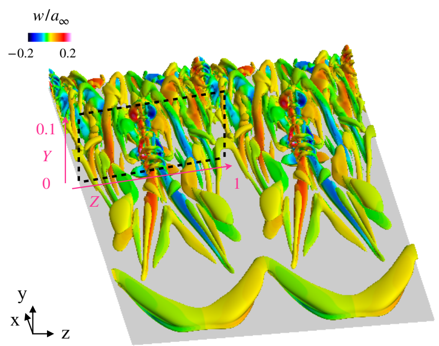

Figure 5. Late stage of the H-type transition, visualized by the iso-surfaces of Q criterion colored by spanwise velocity.

CONCLUSIONS

In this study, we proposed a data-driven input-output analysis framework, called the forcing-informed (FI) resolvent analysis, that extracts the input-output relations in the nonlinear (statistically stationary) flows. The proposed method focused on the physical significance of the nonlinear forcing term appearing in the perturbation equation derived from the Navier–Stokes equations, which plays a critical role in sustaining the oscillatory motions of nonlinear flows. To incorporate the forcing information into the proposed method, the input and output subspaces derived from their respective snapshot data were introduced, and their basis vectors were numerically obtained. The estimated bases and linear operator were used to construct the FI resolvent operator (transfer function) that encodes the input-output relations in the nonlinear flow of in-

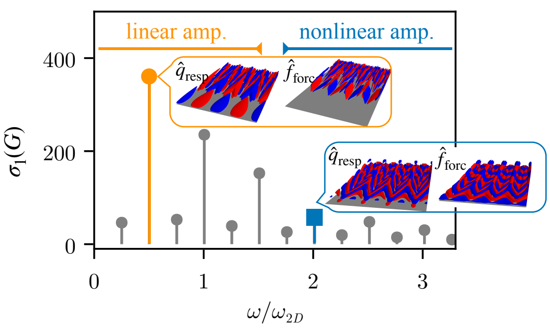

Figure 6. Gains of the FI resolvent operator G, along with the iso-contours of the streamwise component of the response and forcing modes.

terest. At the same time, the snapshot datasets of the input and output are also used to estimate the linear time-invariant operator, enabling the fully data-driven computation of the FI resolvent operator. The forcing and response modes extracted by the proposed method are expressed as linear combinations of the basis vectors of the output and input subspaces, ensuring that the modes lie within the actual flow field.

The proposed method was applied to a two-dimensional cylinder flow and a three-dimensional transitional boundary layer. In both cases, the nonlinear amplification mechanism, which the conventional resolvent analysis fails to predict, was captured through the gain of the FI resolvent operator. By learning the basis of the input subspace, the forcing mode was confined to the region where the response mode emerges, thereby forming the feedback mechanisms crucial for a self-sustaining mechanism. In addition, examining the phase difference between the FI response and forcing modes clarified the role of the FI forcing mode in the self-sustaining mechanism, i.e., whether it amplifies or attenuates fluctuation energy. Further details of the proposed method will be reported in Iwatani *et al.* (2026).

ACKNOWLEDGMENT

This work was supported in part by the Japan Society for the Promotion of Science (JSPS) Grant-in-Aid for JSPS Fellows JP23KJ0167 and by JSPS KAKENHI Grant Number

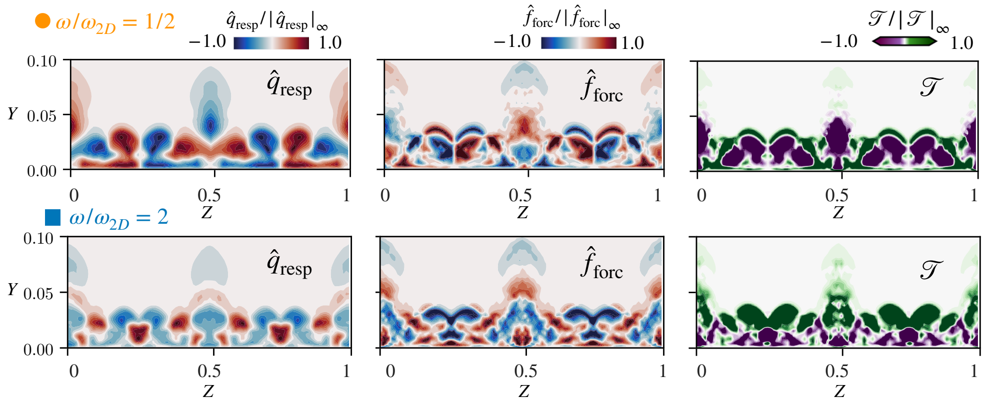

Figure 7. Results of the FI resolvent analysis of the transitional boundary layer: (left) streamwise momentum component of FI forcing, (middle) FI response modes, and (right) the spatial distribution of $\mathscr{T}$, at $\omega/\omega_{2D} = 1/2$ (top) and 2 (bottom).

26H02169. Computer resources of the Fugaku supercomputer were provided by the RIKEN Advanced Institute for Computational Science through the HPCI System Research project (project ID hp240083, hp250090,hp260108). KT acknowledges the Vannevar Bush Faculty Fellowship. YI thanks Dr. Manami Fujii for valuable comments on this proceeding.

REFERENCES

Asada, H & Kawai, S 2025 Exact parallelized dynamic mode decomposition with Hankel matrix for large-scale flow data. *Theor. Comput. Fluid Dyn.* **39** (1), 1–36.

Ballouz, E, Lopez-Doriga, B, Dawson, S T M & Bae, H J 2024 Wavelet-based resolvent analysis of non-stationary flows. *J. Fluid Mech.* **999** (A53), A53.

Barthel, B, Zhu, X & McKeon, B 2021 Closing the loop: nonlinear Taylor vortex flow through the lens of resolvent analysis. *J. Fluid Mech.* **924**.

Farrell, Brian F & Ioannou, Petros J 1993 Stochastic forcing of the linearized Navier–Stokes equations. *Phys. Fluids* **5** (11), 2600–2609.

Gómez, F, Blackburn, H M, Rudman, M, Sharma, A S & McKeon, B J 2016 A reduced-order model of three-dimensional unsteady flow in a cavity based on the resolvent operator. *J. Fluid Mech.* **798**.

Herbert, T 1983 Secondary instability of plane channel flow to subharmonic three-dimensional disturbances. *Phys. Fluids* **26** (4), 871–874.

Herrmann, B, Baddoo, P, Semaan, R, Brunton, S. L. & McKeon, B. J. 2021 Data-driven resolvent analysis. *J. Fluid Mech.* **918**.

Iwatani, Y, Asada, H & Kawai, S 2025 Direct numerical simulation of subharmonic transition in pseudo-adiabatic, heated and cooled boundary layers at Mach number 0.8. *Int. J. Heat Fluid Flow* **116** (109896).

Iwatani, Y, Asada, H, Yeh, C.-A, Taira, K & Kawai, S 2023 Identifying the self-sustaining mechanisms of transonic airfoil buffet with resolvent analysis. *AIAA J.* **61** (6), 2400–2411.

Iwatani, Y, Taira, K & S, Kawai 2026 Forcing-informed resolvent analysis: Identification of input-output relations in self-sustained flows. In preparation.

Jin, B, Symon, S & Illingworth, S J 2021 Energy transfer mechanisms and resolvent analysis in the cylinder wake. *Phys. Rev. Fluids* **6** (2), 024702.

Jovanović, M R & Bamieh, B 2005 Componentwise energy amplification in channel flows. *J. Fluid Mech.* .

Mack, L. M 1975 Linear stability theory and the problem of supersonic boundary-layer transition. *AIAA J.* **13** (3), 278–289.

McKeon, B J & Sharma, A S 2010 A critical-layer framework for turbulent pipe flow. *J. Fluid Mech.* **658**, 336–382.

Morra, Pierluigi, Nogueira, Petrônio A S, Cavalieri, André V G & Henningson, Dan S 2021 The colour of forcing statistics in resolvent analyses of turbulent channel flows. *J. Fluid Mech.* **907** (A24), A24.

Nogueira, Petrônio A S, Morra, Pierluigi, Martini, Eduardo, Cavalieri, André V G & Henningson, Dan S 2021 Forcing statistics in resolvent analysis: application in minimal turbulent Couette flow. *J. Fluid Mech.* **908**, A32.

Rosenberg, K, Symon, S & McKeon, B J 2019 Role of parasitic modes in nonlinear closure via the resolvent feedback loop. *Phys. Rev. Fluids* **4** (5), 052601.

Schmid, P J 2010 Dynamic mode decomposition of numerical and experimental data. *J. Fluid Mech.* **656**, 5–28.

Taira, K, Brunton, Steven L, Dawson, S T M, Rowley, C W, Colonius, T, McKeon, B J, Schmidt, O T, Gordeyev, S, Theofilis, V & Ukeiley, L S 2017 Modal analysis of fluid flows: An overview. *AIAA J.* **55** (12), 4013–4041.

Taira, K, Hemati, M. S, Brunton, S. L, Sun, Y, Duraisamy, K, Bagheri, S, Dawson, S T M & Yeh, C.-A 2020 Modal analysis of fluid flows: Applications and outlook. *AIAA J.* **58** (3), 998–1022.

Towne, A, Schmidt, O. T & Colonius, T 2018 Spectral proper orthogonal decomposition and its relationship to dynamic mode decomposition and resolvent analysis. *J. Fluid Mech.* **847**, 821–867.

Trefethen, L N, Trefethen, A E, Reddy, S C & Driscoll, T A 1993 Hydrodynamic stability without eigenvalues. *Science* **261** (5121), 578–584.

Welch, P 2003 The use of fast Fourier transform for the estimation of power spectra: A method based on time averaging over short, modified periodograms. *IEEE Trans. Audio Electroacoust.* **15** (2), 70–73.

Yeh, C.-A, Benton, S I, Taira, K & Garmann, D J 2020 Resolvent analysis of an airfoil laminar separation bubble at Re=500000. *Phys. Rev. Fluids* **5** (8).

Zare, Armin, Jovanović, Mihailo R & Georgiou, Tryphon T 2017 Colour of turbulence. *J. Fluid Mech.* **812**, 636–680.